communications materials | Article

A Nature Portfolio journal

https://doi.org/10.1038/s43246-026-01175-0

Impact of electron correlations on infinite-layer cuprates and nickelates

Check for updates

Xunyang Hong[1,2,13], Yuetong Wu[1,3,13], Izabela Biało[2], Ying Chan[1,3], Sze Tung Li[1], Leonardo Martinelli[2], Orion Gerguri[2,4], Annabella Drewanowski[2], Qiang Gao[5], Xiaolin Ren[5], Xingjiang Zhou[5], Zhihai Zhu[5], Alice Galdi[6,7], Darrell G. Schlom[7,8], Kyle M. Shen[8,9], Jaewon Choi[10], Mirian Garcia-Fernandez[10], Ke-Jin Zhou[10], Nicholas B. Brookes[11], Henrik M. Rønnow[12], Qisi Wang[1,3] ✉ & Johan Chang[2]

Optimization of unconventional superconductivity involves a balance of interaction strengths. Precise determination of correlation strength across different material families is therefore important. Here, we present a combined X-ray absorption spectroscopy (XAS) and resonant inelastic X-ray scattering (RIXS) study of infinite-layer $PrNiO_2$ and $SrCuO_2$ that enables fair comparison of their interaction strengths. For both compounds, we study the orbital and magnetic excitations and extract their dispersions along high-symmetry directions. Using a single-band Hubbard model and including physically plausible assumptions about higher-order exchange interactions, we estimate the correlation factor U/t for both compounds. A key finding is that despite the prediction of a smaller Coulomb repulsion U, $PrNiO_2$ exhibits a correlation strength U/t that is 20% stronger than that of its isostructural cuprate counterpart $SrCuO_2$. This indicates that moderation of the correlation strength may further optimize superconductivity in nickelates.

The discovery of superconductivity in doped and undoped infinite-layer nickelates has stimulated new research lines[1–3]. One important question is whether there exists a mapping between cuprate and nickelate superconductivity. Similar orbital motives exist in both compound families. Like cuprates, infinite-layer nickelates exhibit a layered structure with a $3d^9$ electronic configuration, where holes occupy the $d_{x^2-y^2}$ shell and strong electronic correlations are present[4,5]. However, key distinctions emerge, particularly in their electronic structure[6] and magnetic properties, posing significant challenges to our understanding[7]. One critical aspect that may distinguish the underlying physics between nickelates and cuprates is the strength of electron correlations, characterized by the ratio between the on-site Coulomb repulsion U to the nearest-neighbour hopping integral t (i.e. U/t). Within the framework of single-band Hubbard models — widely used to describe correlated behaviors in both nickelates and cuprates — U/t governs the balance between magnetic ordering and superconductivity[8,9]. Unconventional superconductivity emerges from these correlations, but localization effects dominate in the strong-coupling limit.

Experimental attempts have been made to characterize the electronic structure and correlation effects in infinite-layer nickelates. These include angle-resolved photoemission spectroscopy (ARPES)[10–12], X-ray absorption spectroscopy (XAS)[13], X-ray photoemission spectroscopy (XPS)[14], resonant inelastic X-ray scattering (RIXS)[15,16], and electron energy-loss spectroscopy (EELS)[6,17]. Yet, a quantitative conclusion remains elusive due to different types of experimental limitations. The study of collective spin excitations offers an alternative approach, as the superexchange couplings originate from electronic correlation effects. A recent RIXS study compared magnons in $NdNiO_2$ and $YBa_2Cu_3O_{7-\delta}$[18]. Using a single-band Hubbard model, this work concluded that the Coulomb repulsion U of $NdNiO_2$ is twice that of $YBa_2Cu_3O_{7-\delta}$, leading to a 60% larger U/t in the nickelates. However, this methodology has some shortcomings. First, recent ARPES results have revealed a circular Fermi surface[10–12], suggesting that next-nearest-neighbor

[1]Department of Physics, The Chinese University of Hong Kong, Shatin, Hong Kong, China. [2]Physik-Institut, Universität Zürich, Zürich, Switzerland. [3]State Key Laboratory of Quantum Information Technologies and Materials, The Chinese University of Hong Kong, Shatin, Hong Kong, China. [4]PSI Center for Neutron and Muon Sciences CNM, Villigen, PSI, Switzerland. [5]Beijing National Laboratory for Condensed Matter Physics, Institute of Physics, Chinese Academy of Sciences, Beijing, China. [6]Dipartimento di Ingegneria Industriale, Universita' degli Studi di Salerno, Fisciano, SA, Italy. [7]Department of Materials Science and Engineering, Cornell University, Ithaca, NY, USA. [8]Kavli Institute at Cornell for Nanoscale Science, Ithaca, NY, USA. [9]Department of Physics, Laboratory of Atomic and Solid State Physics, Cornell University, Ithaca, NY, USA. [10]Diamond Light Source, Harwell Campus, Didcot, OX11 0DE, United Kingdom. [11]European Synchrotron Radiation Facility, Grenoble, France. [12]Institute of Physics, École Polytechnique Fedérale de Lausanne (EPFL), Lausanne, Switzerland. [13]These authors contributed equally: Xunyang Hong, Yuetong Wu. ✉e-mail: qwang@cuhk.edu.hk

hopping (t') plays a significant role. Second, the compared nickelate and cuprate compounds were not isostructural. The presence of apical oxygen in cuprates is known to suppress longer-range hopping and exchange processes[19,20], which further hinders a fair comparison.

To facilitate a direct comparison, we conducted a resonant inelastic X-ray scattering (RIXS) study on $PrNiO_2$, mapping out its electronic and magnetic excitations across high-symmetry directions. Our data extend beyond the scope of previous studies, providing a comprehensive characterization of the *k*-space properties of magnetic and orbital excitations. By incorporating higher-order hopping terms t' and t'', and considering a magnon renormalization that depends on electron correlation in our analysis, we extract refined values for U and t from our experimental data. These results also allow us to characterize charge fluctuations and staggered magnetization with greater accuracy. We further compare these results with those obtained on the isostructural infinite-layer cuprate $SrCuO_2$ thin film, analyzed with the same approach. This direct comparison reveals a 20% stronger correlation strength U/t in $PrNiO_2$ compared to $SrCuO_2$. Our analysis of the orbital excitations further indicates a reduced orbital exchange in $PrNiO_2$ resulting from stronger electronic localization. Implications for electronic properties such as staggered magnetic moments, superconductivity, and strange metal properties are discussed.

Results

X-ray absorption spectra (XAS) using vertical incident light polarization across the nickel and copper L_3-edges — shown in Fig. 1 — are shown for our $PrNiO_2$ and $SrCuO_2$ films. A significant linear dichroism is observed in the XAS of $PrNiO_2$ at grazing-incidence geometry (see Supplementary Information). The enhanced absorption peak for σ incident X-rays indicates a dominant contribution from the in-plane $d_{x^2-y^2}$ orbital. The RIXS energy tuning map — shown in Fig. 1b — reveals that magnetic and orbital excitations are resonating at the Ni L-edge. RIXS spectra recorded on $SrCuO_2$ and $PrNiO_2$ at the Cu and Ni L_3-edges are shown in Fig. 1e and 1f. For both compounds, the *dd* orbital excitations are the most intense and a weaker magnon excitation is observed near the elastic line. The *dd* excitations are analyzed and indexed according to the d-orbital level splitting in a square-planar crystal-field environment for both $SrCuO_2$ and $PrNiO_2$. An additional excitation at 0.7 eV in $PrNiO_2$ has been attributed to the hybridization between Ni 3d and Pr 5d states[15,21]. Consistent with an earlier report on isostructural $CaCuO_2$[22], the d_{xy} orbital excitation displays a significant dispersion in $SrCuO_2$. For $PrNiO_2$, this collective behavior is not detectable within the experimental resolution.

In Fig. 2, we focus on the low-energy part of the RIXS spectra recorded near high-symmetry zone-boundary points with σ and π polarizations, which enhance the phonon and single-magnon cross-sections, respectively. The spectra with π polarization are analysed using a five-component model. Gaussian profiles are used for the elastic scattering (grey shaded area), and two phonon modes (blue shades)[23]. A damped harmonic oscillator function[24] is applied to model the magnon modes. The background is modeled by a quadratic function. Note that the optical phonon mode around 80 meV becomes stronger at lower Q, leading to a sharp peak-like feature overlapping with the magnon near (0, 0) (see Supplementary Fig. 3 for representative fits). From the damped magnon excitation (see Supplementary Information), we extract the magnon dispersion — see Figs. 2e and 3d–f.

Analysis

Before providing a refined analysis of the magnon dispersions, we emphasize the key observables and their implications. The magnon bandwidth in $PrNiO_2$ (~ 180 meV) is half that of $SrCuO_2$ (~ 360 meV), revealing a weaker nearest-neighbour exchange coupling $J_1 \sim t^2/U$. We find that the magnon zone boundary dispersion — defined by the energy difference between (0.5, 0) and (0.25, 0.25) — is comparatively stronger in $SrCuO_2$. Similarly, the d_{xy} orbital excitation exhibits a stronger dispersion (~ 80 meV) in $SrCuO_2$. Within a single-band Hubbard model, the zone-boundary magnon dispersion is dictated by a series of higher-order exchange terms such as t^4/U^3, t'^2/U, and t''^2/U which gain prominence when the correlation U/t decreases. In a strong-coupling scenario, the d_{xy} dispersion originates from higher-order orbital superexchange terms[22]. Thus, these observations

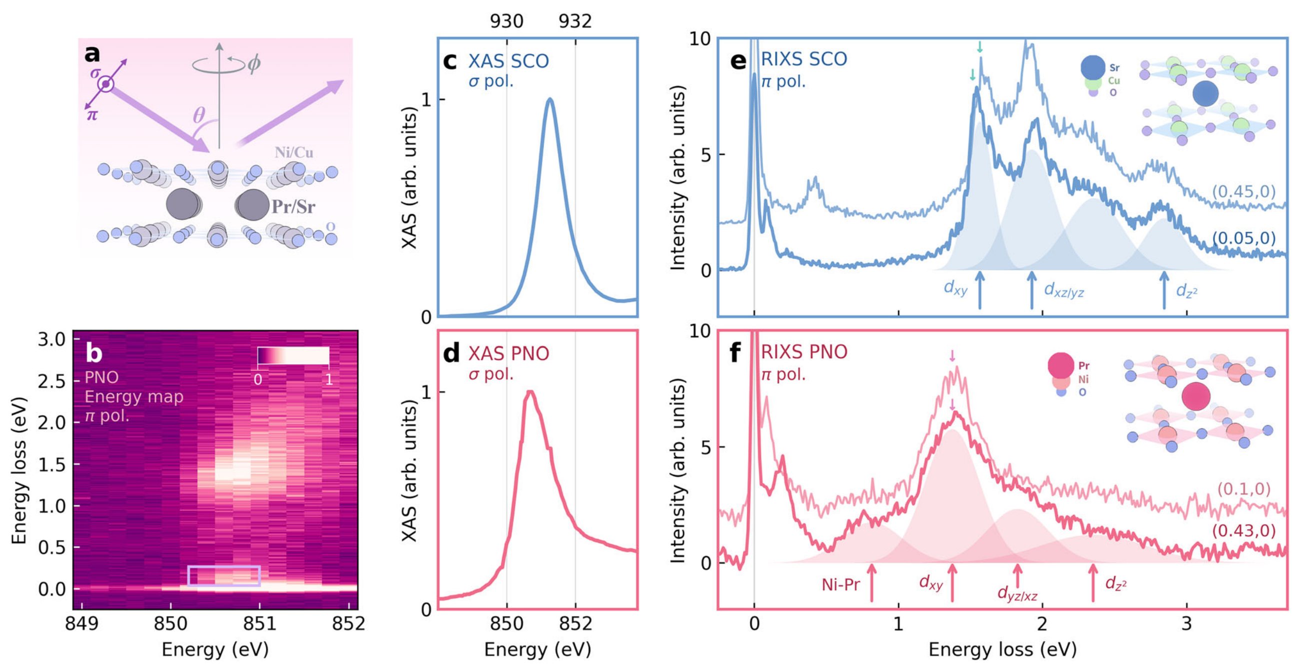

Fig. 1 | X-ray absorption spectroscopy (XAS) and resonant inelastic X-ray scattering (RIXS) on $SrCuO_2$ and $PrNiO_2$ films. a Schematic illustration of the RIXS scattering geometry — with θ describing the incident angle and ϕ the sample rotation. σ and π indicate respectively linear horizontal and vertical incident light polarizations. **b** RIXS energy map recorded on $PrNiO_2$. The purple rectangle inset marks the resonant magnon intensity. **c**, **d** Cu L-resonance of $SrCuO_2$ and Ni L-resonance of $PrNiO_2$ probed with XAS (**e**, **f**) RIXS spectra recorded on $SrCuO_2$ and $PrNiO_2$ at respectively the Cu and Ni L-edges and at in-plane momentum transfers as indicated. Small down-pointing arrows mark the shift (marginal-shift) of d_{xy} excitations in $SrCuO_2$ ($PrNiO_2$). Modeling of the crystal field excitations are indicated with shaded Gaussian profiles. The insets illustrate the equivalent crystal structure of $SrCuO_2$ and $PrNiO_2$.

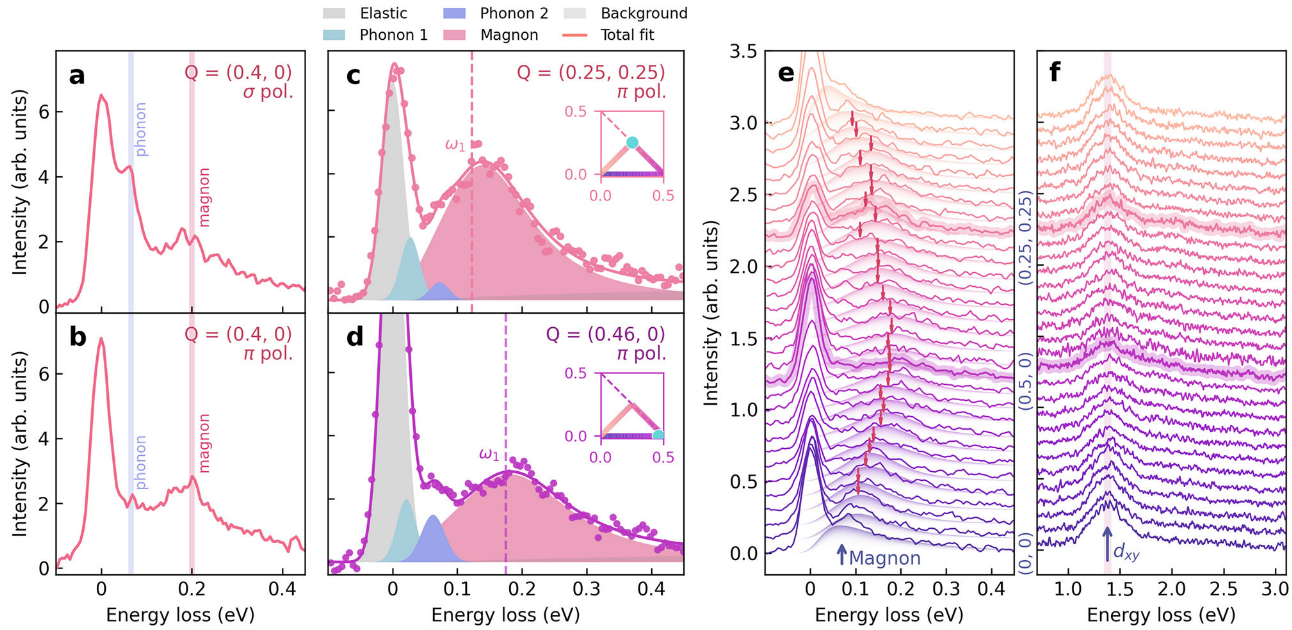

Fig. 2 | RIXS spectroscopy of infinite layer $PrNiO_2$. **a**, **b** Representative RIXS spectra of $PrNiO_2$ with polarization as indicated. Vertical lines mark the phonon and magnon modes. **c**, **d** RIXS spectra recorded with π polarization on $PrNiO_2$ at two high-symmetry zone boundary points as depicted in the insets. The modeling fits are described in the text. Grey component covers elastic scattering and the two blue components are interpreted as phonon excitations. Red shaded areas model the magnetic excitations. Vertical dashed lines indicate the magnon damped energy ω_1 (see Supplementary Information). **e**, **f** RIXS spectra of $PrNiO_2$ along three high-symmetry directions. Red arrows in (**e**) indicate the dispersion of magnon damped energy ω_1 of the fits. Vertical line in (**f**) is a guide to the eye.

suggest that higher-order terms are more pronounced in $SrCuO_2$, leading to the conclusion that $PrNiO_2$ is more correlated compared to $SrCuO_2$. The question is by how much.

Having extracted the magnon dispersion of $PrNiO_2$ and compared it with isostructural $SrCuO_2$, we now turn to discuss the effective spin exchange interactions. Magnon excitations in cuprates have previously been analysed using a single-band Hubbard model projected into a Heisenberg Hamiltonian[25–29]. These studies include analysis of La_2CuO_4, that on the energy scales of U and $4t$, is not strictly a single-band system[30,31]. We are therefore extending the analysis to $PrNiO_2$, which, like La_2CuO_4, hosts both dominant $d_{x^2-y^2}$ and other orbital (presumably interstitial s) states at the Fermi level[12]. Generally, exchange interactions are parameterized through the Coulomb interaction U and nearest neighbor hoppings t, t' and t''. To make a comparative analysis, we here assume that $SrCuO_2$'s and $PrNiO_2$'s dimensionless ratios of square lattice hopping parameters t'/t and t''/t' are comparable. An identical and significant t'/t ratio has been suggested for infinite-layer nickelates and cuprates by first-principles calculations[5], although the magnitudes of hopping amplitudes (and hence the energy scale) can differ substantially from the experimentally observed values. Accordingly, in the following we fix the dimensionless ratios, but allow the overall hopping scale to vary. Specifically, we use the ratios found for cuprates — that is, $t'/t = -0.4$[30] and $t''/t' = -0.5$[32]. The $t'/t \approx -0.4$[30,33,34] value is generally used across layered cuprates irrespective of the apical oxygen distance. As such, this ratio is also expected to be relevant for infinite-layer cuprates.

Within this formalism, zone boundary dispersion — as observed in both $PrNiO_2$ and $SrCuO_2$ — implies non-negligible higher-order exchange interaction terms[25–28]. In a recent work on $SrCuO_2$, it was shown that such high-order terms alone are insufficient in describing the zone boundary dispersion found in $SrCuO_2$[35]. To account for the observed magnon dispersion, a self-consistent evaluation of the magnon renormalization factor Z is required. This implies that the magnon dispersion is described by the product of momentum dependent energy ω_k and momentum dependent renormalization factor Z_k. The larger zone boundary dispersion observed for $SrCuO_2$ implies that this compound has a more pronounced momentum dependence of Z_k. Larger zone boundary dispersion stems from higher-order exchange interaction terms that in turn control Z_k[27,28]. Applying this model to $PrNiO_2$ and $SrCuO_2$, it is possible to derive a direct comparison between the nickelates and cuprates. The obtained momentum dependence of Z_k is shown in Fig. 3a-c. The results of our parametrization are given in Table 1. Overall, we find that the Coulomb interaction U is lower (by 25–30%) in $PrNiO_2$ compared to $SrCuO_2$. However, the correlation parameter U/t is about 20% stronger in $PrNiO_2$.

Discussion

Although RIXS experiments have revealed collective spin excitations that persist across a wide doping range of infinite-layer nickelates[16,21,36], their intrinsic ground states remain elusive. Current experimental characterizations of undoped compounds suggest either a weakly insulating or superconducting state[2,3,37], with some evidence for spin-glass behavior[38–41]. However, it is still unclear whether the absence of long-range magnetic order in bulk $PrNiO_2$ arises from self-doping or is influenced by sample synthesis conditions[38,39,42]. Recent studies have further complicated the picture: a muon spin rotation (μSR)[43] and an X-ray magnetic circular dichroism (XMCD) experiment[44] reported evidence for local magnetic moments from Ni^+ ions in thin films, whereas inelastic neutron scattering measurements of bulk $LaNiO_2$ single crystals failed to observe spin fluctuations[45]. These conflicting experimental results further complicate the intrinsic magnetic ground state in these systems.

In this context, an estimate of the staggered magnetization $\langle M_s \rangle$ from the spin excitations would provide insights into this question. For Mott insulating antiferromagnets, the staggered magnetization $\langle M_s \rangle$ is defined by the effective spin number but can be reduced by charge fluctuations. In La_2CuO_4, spin-wave calculations using a Hubbard model that includes first to third nearest neighbor hopping integrals gives a $\langle M_s \rangle$ very close to the value obtained from neutron diffraction measurements[27]. Our recent RIXS study of $SrCuO_2$ has shown that further decreasing the correlation strength U/t will disrupt the Néel order and induce other magnetic ground states[35]. This analysis thus provides an effective experimental approach to infer the magnetic ground state by analyzing the spin excitations. From the extracted electronic parameters of $PrNiO_2$, we obtain $\langle M_s \rangle \simeq 0.117$ (see Methods),

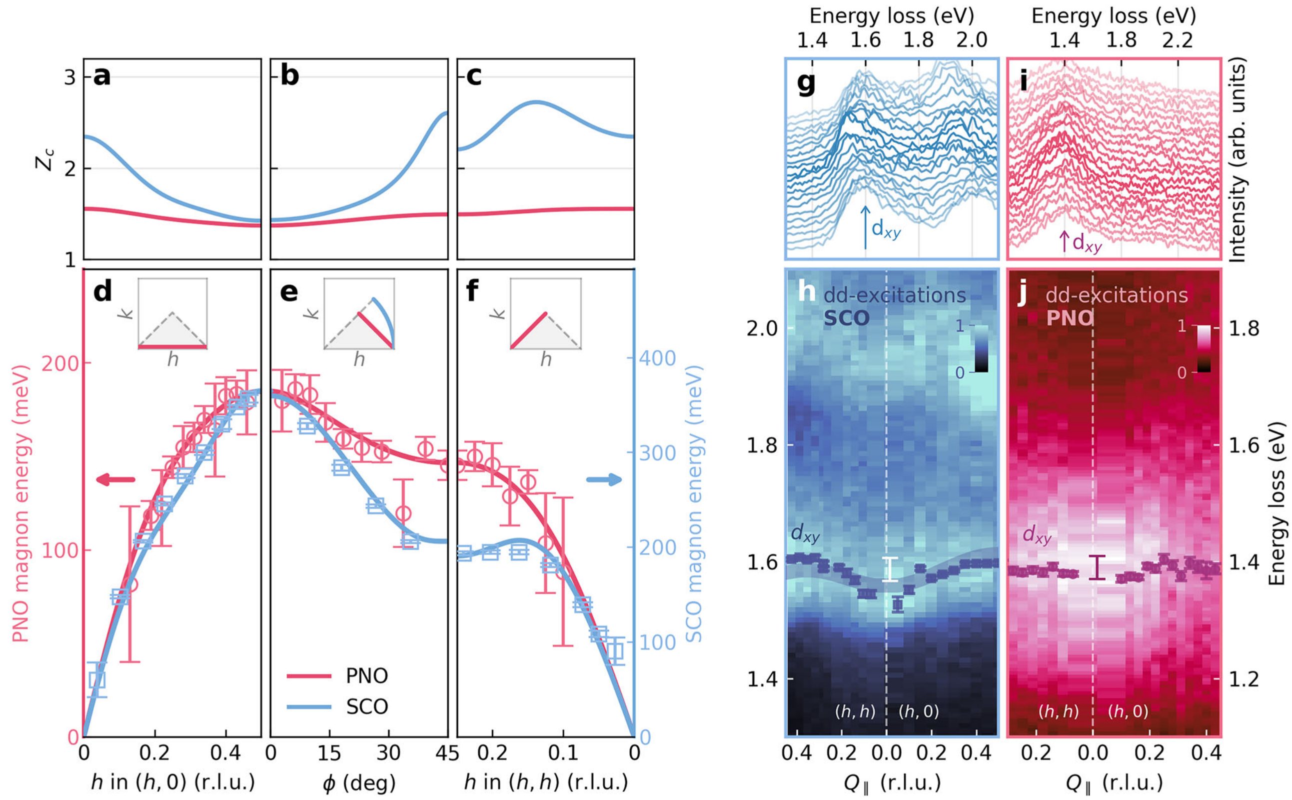

Fig. 3 | Dispersion of magnons in $PrNiO_2$ and $SrCuO_2$. **a**–**c** Renormalization factor Z_c for $PrNiO_2$ (red) and $SrCuO_2$ (blue) along the momentum trajectories indicated in the corresponding insets of (**d**–**f**). **d**–**f** Dispersions of magnons for $PrNiO_2$ (left y-axis, red) and $SrCuO_2$ (right y-axis, blue). Symbols represent measured data with error bars, and solid lines are fits. Insets in (**d**–**f**) show the momentum path in the Brillouin zone for each case. In (**b**) and (**e**), the two samples follow different trajectories, as highlighted in the inset. Therefore, we use azimuthal angles ϕ to label the momentum transferred. **g**, **i** RIXS spectra — recorded along the $(h, 0)$ and (h, h) directions for $SrCuO_2$ and $PrNiO_2$ — concentrating on the *dd* excitations. Vertical gray lines are visual guides to the eye. **h**, **j** Same data as in (**g**, **i**) but represented in a false color-map format. Dots are center of the Gaussian fits of the d_{xy} excitations. Vertical bars indicate the experimental energy resolutions.

Table 1 | Electronic parameters *t* and *U* for $PrNiO_2$ and cuprate systems as indicated

Sample	*t* [meV]	*U* [eV]	*U*/*t*	Ref.
LCO/STO	408	3.38	8.3	35
PNO/STO	**247**	**2.0**	**8.1**	This work
Tl2504	372	2.57	6.9	49
CCO	500	3.39	6.8	35
SCO/GSO	**431.5**	**2.68**	**6.2**	This work,[35]

These parameters are extracted from a single-band Hubbard model projected into a Heisenberg Hamiltonian from which the observed magnon dispersion is fitted. For this fit, we assume $t'/t = -0.4$ (realistic for cuprates[30]) and $t''/t' = -0.5$[32].

which is smaller than $\langle M_s \rangle \simeq 0.235$ of La_2CuO_4[27], but larger than that of $SrCuO_2$[35].

The strength of electronic correlations significantly influences unconventional superconductivity. Recent theoretical studies on single-band Hubbard model using dynamical vertex approximation (DΓA) and density functional theory (DFT) calculations demonstrated that T_c exhibits a dome-like dependence on U/t[8,9]. Excessively strong electronic correlations suppress superconductivity by enhancing antiferromagnetic fluctuations, which open a pseudogap and weaken the electron propagator. Optimal T_c is achieved at intermediate coupling ($U/t \approx$ 6-7). The larger U/t in $PrNiO_2$ compared to $SrCuO_2$ places it outside this optimum, which may account for its lower T_c. This aligns with our finding that undoped $PrNiO_2$ may host a larger staggered magnetization compared to $SrCuO_2$. Notably, it has been further suggested that reducing U/t via external pressure or compressive strain can shift nickelates toward the optimal correlation range[46,47]. This is consistent with the observation of T_c enhancement from 17 K to over 30 K in $Pr_{0.82}Sr_{0.18}NiO_2$ thin films under hydrostatic pressures[48]. A recent study on cuprates also reveals the critical role of moderate correlation strength in optimizing T_c[49]. Regardless of the correlation and superconducting pairing strength, both cuprates and infinite-layer nickelates exhibit strange metal behaviour around optimal doping[37,50,51]. Overall, their normal state electronic properties share common characteristics, suggesting similar essential physics despite the variation in correlation strength.

Note added. Upon completion of this work, we became aware of an independent RIXS study of magnetic and orbital excitations in infinite-layer nickelate and cuprate films[52].

Methods

RIXS experiments

Thin films of the $PrNiO_2$ on $SrTiO_3$ (STO) substrates are prepared following procedures described in Ref. 21. Ni *L*-edge (~ 850.6 eV) RIXS experiments were performed at the I21 beamline of the Diamond Light Source (DLS)[53]. The energy resolution, determined by the full-width-at-half-maximum of the elastic scattering profile of a carbon tape, was set to 39 meV. The scattering angle was fixed to 154°, and the sample temperature was set to 16 K. Cu *L*-edge (~ 931 eV) RIXS experiments on thin films of $SrCuO_2$ grown on $GdScO_3$ (GSO) substrates were carried out at the ADRESS and ID32 beamlines at respectively the Swiss Light Source (SLS) and the European Synchrotron Radiation facility (ESRF)[54]. Experiments at ID32 were performed with an energy resolution of 39.5 meV and a scattering angle of 145°, at a sample temperature of 25 K. Momentum transfer is indexed in reciprocal lattice units (r.l.u.) of the tetragonal unit cell. Experiments at the ADRESS beamline have previously been described in Ref. 35. All RIXS spectra are normalized to the area of the *dd* excitations (700-4000 meV).

Magnon analysis

Magnon dispersions are fitted using a single-band Hubbard model by calculating self-consistently Z_c and ϵ_k in $\hbar\omega = Z_c(U, t, t', t'')\epsilon_k(U, t, t', t'')$. Here, $\epsilon_k(U, t, t', t'') = \sqrt{A_k^2 - B_k^2}$ is the bare magnon dispersion with A_k and B_k determined by U, t, t', and t'', and renormalization factor Z_c is calculated by considering the magnon-magnon interaction, as described in Refs. 27, 28, 35, 49. We assume $t'/t = -0.4$[30] and $t''/t' = -0.5$[32]. Parameters U and t are obtained by a least-squares fit. The staggered magnetization is calculated by $\langle M_s \rangle = (S + \frac{1}{2} - \frac{2}{N}\sum_\mathbf{k} \frac{A_\mathrm{k}}{2\epsilon_\mathrm{k}})(1 - 8t^2/U^2)$, where N is the number of spin ($S = 1/2$) on the square lattice.

Data availability

Data reported here are available from the corresponding author upon request.

Received: 10 December 2025; Accepted: 22 April 2026;
Published online: 07 May 2026

References

1. Li, D. et al. Superconductivity in an infinite-layer nickelate. *Nature* **572**, 624 (2019).
2. Parzyck, C. T. et al. Superconductivity in the parent infinite-layer nickelate $NdNiO_2$. *Phys. Rev. X* **15**, 021048 (2025).
3. Sahib, H. et al. Superconductivity in $PrNiO_2$ infinite-layer nickelates. *Adv. Mater*. **37**, 2416187 (2025).
4. Anisimov, V. I., Bukhvalov, D. & Rice, T. M. Electronic structure of possible nickelate analogs to the cuprates. *Phys. Rev. B* **59**, 7901 (1999).
5. Botana, A. S. & Norman, M. R. Similarities and differences between $LaNiO_2$ and $CaCuO_2$ and implications for superconductivity. *Phys. Rev. X* **10**, 011024 (2020).
6. Goodge, B. H. et al. Doping evolution of the Mott-Hubbard landscape in infinite-layer nickelates. *Proc. Natl. Acad. Sci. USA*. **118**, e2007683118 (2021).
7. Ghiringhelli, G. A noticeable absence. *Nat. Mater.* **23**, 443 (2024).
8. Kitatani, M. et al. Optimizing superconductivity: From cuprates via nickelates to palladates. *Phys. Rev. Lett.* **130**, 166002 (2023).
9. Worm, P. et al. Spin fluctuations sufficient to mediate superconductivity in nickelates. *Phys. Rev. B* **109**, 235126 (2024).
10. Ding, X. et al. Cuprate-like electronic structures in infinite-layer nickelates with substantial hole dopings. *Natl. Sci. Rev.* **11**, nwae194 (2024).
11. Sun, W. et al. Electronic structure of superconducting infinite-layer lanthanum nickelates. *Sci. Adv.* **11**, adr5116 (2025).
12. Li, C. et al. Observation of electridelike *s* states coexisting with correlated *d* electrons in $NdNiO_2$. *Phys. Rev. Lett.* **135**, 116501 (2025).
13. Xiao, W. et al. Superconductivity in an infinite-layer nickelate superlattice. *Nat. Commun.* **15**, 10215 (2024).
14. Chen, Z. et al. Electronic structure of superconducting nickelates probed by resonant photoemission spectroscopy. *Matter* **5**, 1806 (2022).
15. Hepting, M. et al. Electronic structure of the parent compound of superconducting infinite-layer nickelates. *Nat. Mater.* **19**, 381 (2020).
16. Lu, H. et al. Magnetic excitations in infinite-layer nickelates. *Science* **373**, 213 (2021).
17. Hu, K. et al. Atomic scale disorder and reconstruction in bulk infinite-layer nickelates lacking superconductivity. *Nat. Commun.* **15**, 5104 (2024).
18. Rosa, F. et al. Spin excitations in $Nd_{1-x}Sr_xNiO_2$ and $YBa_2Cu_3O_{7-\delta}$: The influence of Hubbard *U*. *Phys. Rev. B* **110**, 224431 (2024).
19. Peng, Y. Y. et al. Influence of apical oxygen on the extent of in-plane exchange interaction in cuprate superconductors. *Nat. Phys.* **13**, 1201 (2017).
20. Wang, Y., Huang, E. W., Moritz, B. & Devereaux, T. P. Magnon splitting induced by charge transfer in the three-orbital Hubbard model. *Phys. Rev. Lett.* **120**, 246401 (2018).
21. Gao, Q. et al. Magnetic excitations in strained infinite-layer nickelate $PrNiO_2$ films. *Nat. Commun.* **15**, 5576 (2024).
22. Martinelli, L. et al. Collective nature of orbital excitations in layered cuprates in the absence of apical oxygens. *Phys. Rev. Lett.* **132**, 066004 (2024).
23. Hong, X. et al. Observation of collective charge excitations in a cuprate superconductor. *arXiv:2503.04334* (2025).
24. Lamsal, J. & Montfrooij, W. Extracting paramagnon excitations from resonant inelastic x-ray scattering experiments. *Phys. Rev. B* **93**, 214513 (2016).
25. Coldea, R. et al. Spin waves and electronic interactions in La_2CuO_4. *Phys. Rev. Lett.* **86**, 5377 (2001).
26. Headings, N. S., Hayden, S. M., Coldea, R. & Perring, T. G. Anomalous high-energy spin excitations in the high-T_c superconductor-parent antiferromagnet La_2CuO_4. *Phys. Rev. Lett.* **105**, 247001 (2010).
27. Delannoy, J.-Y. P., Gingras, M. J. P., Holdsworth, P. C. W. & Tremblay, A.-M. S. Low-energy theory of the *t-t'-t"-U* Hubbard model at half-filling: Interaction strengths in cuprate superconductors and an effective spin-only description of La_2CuO_4. *Phys. Rev. B* **79**, 235130 (2009).
28. Dalla Piazza, B. et al. Unified one-band Hubbard model for magnetic and electronic spectra of the parent compounds of cuprate superconductors. *Phys. Rev. B* **85**, 100508 (2012).
29. Ivashko, O. et al. Strain-engineering Mott-insulating La_2CuO_4. *Nat. Commun.* **10**, 786 (2019).
30. Matt, C. E. et al. Direct observation of orbital hybridisation in a cuprate superconductor. *Nat. Commun.* **9**, 972 (2018).
31. Horio, M. et al. Two-dimensional type-II Dirac fermions in layered oxides. *Nat. Commun.* **9**, 3252 (2018).
32. Yoshida, T. et al. Systematic doping evolution of the underlying Fermi surface of $La_{2-x}Sr_xCuO_4$. *Phys. Rev. B* **74**, 224510 (2006).
33. Sakakibara, H., Usui, H., Kuroki, K., Arita, R. & Aoki, H. Origin of the material dependence of T_c in the single-layered cuprates. *Phys. Rev. B* **85**, 064501 (2012).
34. Sakakibara, H., Usui, H., Kuroki, K., Arita, R. & Aoki, H. Two-orbital model explains the higher transition temperature of the single-layer Hg-cuprate superconductor compared to that of the La-cuprate superconductor. *Phys. Rev. Lett.* **105**, 057003 (2010).
35. Wang, Q. et al. Magnon interactions in a moderately correlated Mott insulator. *Nat. Commun*. **15**, 5348 (2024).
36. Yan, Y. et al. Persistent paramagnons in high-temperature infinite-layer nickelate superconductors. *arXiv:2507.18373*, (2025).
37. Lee, K. et al. Linear-in-temperature resistivity for optimally superconducting (Nd, Sr)NiO_2. *Nature* **619**, 288 (2023).
38. Lin, H. et al. Universal spin-glass behaviour in bulk $LaNiO_2$, $PrNiO_2$ and $NdNiO_2$. *New J. Phys.* **24**, 013022 (2022).
39. Ortiz, R. A. et al. Magnetic correlations in infinite-layer nickelates: An experimental and theoretical multimethod study. *Phys. Rev. Res.* **4**, 023093 (2022).
40. Saykin, D. R. et al. Spin-glass state in nickelate superconductors. *npj Quantum Mater.* **10**, 94 (2025).
41. Zhou, Y. et al. Origin of local magnetic exchange interaction in infinite-layer nickelates. *arXiv:2505.09476* (2025).
42. Li, Q. et al. Absence of superconductivity in bulk $Nd_{1-x}Sr_xNiO_2$. *Commun. Mater.* **1**, 16 (2020).
43. Fowlie, J. et al. Intrinsic magnetism in superconducting infinite-layer nickelates. *Nat. Phys.* **18**, 1043 (2022).
44. Krieger, G. et al. Signatures of canted antiferromagnetism in infinite-layer nickelates studied by x-ray magnetic dichroism. *Phys. Rev. B* **110**, 195110 (2024).
45. Hayashida, S. et al. Lattice dynamics of the infinite-layer nickelate $LaNiO_2$. *Phys. Rev. B* **112**, 205104 (2025).

46. Ren, X. et al. Possible strain-induced enhancement of the superconducting onset transition temperature in infinite-layer nickelates. *Commun. Phys.* **6**, 341 (2023).
47. Lee, Y. et al. Synthesis of superconducting freestanding infinite-layer nickelate heterostructures on the millimetre scale. *Nat. Syn.* **4**, 573 (2025).
48. Wang, N. N. et al. Pressure-induced monotonic enhancement of T_c to over 30 K in superconducting $Pr_{0.82}Sr_{0.18}NiO_2$ thin films. *Nat. Commun.* **13**, 4367 (2022).
49. Biało, I. et al. Magnetic excitations of a half-filled Tl-based cuprate. *arXiv:2507.22242* (2025).
50. Hsu, Y.-T. et al. Transport phase diagram and anomalous metallicity in superconducting infinite-layer nickelates. *Nat. Commun.* **15**, 9863 (2024).
51. Iorio-Duval, C. et al. Quantum criticality at the end of a pseudogap phase in superconducting infinite-layer nickelates. *arXiv:2510.12786* (2025).
52. Rosa, F. et al. Spin and orbital excitations in undoped infinite layers: a comparison between superconducting $PrNiO_2$ and insulating $CaCuO_2$. *arXiv:2511.02448* (2025).
53. Zhou, K.-J. et al. I21: an advanced high-resolution resonant inelastic X-ray scattering beamline at Diamond Light Source. *J. Synchrotron Radiat*. **29**, 563 (2022).
54. Brookes, N. B. et al. The beamline ID32 at the ESRF for soft X-ray high energy resolution resonant inelastic X-ray scattering and polarisation dependent X-ray absorption spectroscopy. *Nucl. Instrum. Methods Phys. Res. A.* **903**, 175 (2018).

Acknowledgements

We thank Kai-Yuan Qi and Dao-Xin Yao for helpful discussions. The work at CUHK is supported by the Research Grants Council of Hong Kong (CUHK 24306223), the Guangdong Provincial Quantum Science Strategic Initiative (GDZX2401012), CUHK Direct Grant (4053671), and the 1+1+1 CUHK-CUHK(SZ)-GDSTC Joint Collaboration Fund (2025A0505000079). X.H., I.B., L.M. and J. Chang thank the Swiss National Science Foundation (Project No. 200021_188564; Spark project CRSK-2_220797). X.H. acknowledges support from UZH Candoc Grant (FK-25-088). L.M. and I.B. acknowledge support from the Swiss Government Excellence Scholarship (ESKAS-Nr: 2023.0052, ESKAS-Nr: 2022.0001) and UZH Postdoc Grants (FK-23-113, FK-23-128). Part of this research from IOP is supported by the National Key Research and Development Program of China (Grant No. 2021YFA1401800 and 2022YFA1403900). The work at Cornell was supported by the National Science Foundation (NSF DMR-2104427) and the Air Force Office of Scientific Research (AFOSR FA9550-21-1-0168 and FA9550-23-1-0161), and made use of the Cornell Center for Materials Research shared instrumentation facility. We acknowledge the DLS and the ESRF for providing beamtime under Proposals MM30189 and HC-5223 at the I21 and ID32 beamlines.

Author contributions

Q.W. and J.Chang conceived the project. Q.G., X.R., X.Z. and Z.Z. grew the $PrNiO_2$ film. A.G. grew and characterized the $SrCuO_2$ film with advice from D.G.S. and K.M.S. X.H., I.B., L.M., O.G., A.D., J.Choi, M.G.F., K.J.Z., N.B.B., Q.W. and J.Chang performed the RIXS experiments. X.H., Y.W., Y.C. and S.T.L. analysed the RIXS data with help from H.M.R. X.H., Q.W. and J.Chang wrote the manuscript with input for other authors.

Competing interests

The authors declare no competing interests.

Additional information

Supplementary information The online version contains supplementary material available at https://doi.org/10.1038/s43246-026-01175-0.

Correspondence and requests for materials should be addressed to Qisi Wang.

Peer review information *Communications Materials* thanks the anonymous reviewers for their contribution to the peer review of this work. A peer review file is available.

Reprints and permissions information is available at http://www.nature.com/reprints

Publisher's note Springer Nature remains neutral with regard to jurisdictional claims in published maps and institutional affiliations.

Supplementary Information for
Impact of Electron Correlations on Infinite-Layer Cuprates and Nickelates

X. Hong *et al.*

I. X-RAY ABSORPTION SPECTROSCOPY

Supplementary Fig. 1 displays the X-ray absorption spectroscopy (XAS) profiles of $PrNiO_2$ measured using total fluorescence yield. The main peak at 850.7 eV corresponds to the Ni L_3-edge resonance, while the shoulder indicated by the arrow is associated with self-doped hole states [1]. At a grazing incidence geometry with an incident angle of $\theta = 10°$, a significant linear dichroism is observed with the main peak being enhanced for σ incident X-rays. This is consistent with previous reports [1, 2], and indicates a dominant contribution from the in-plane $d_{x^2-y^2}$ orbital for the valence electrons.

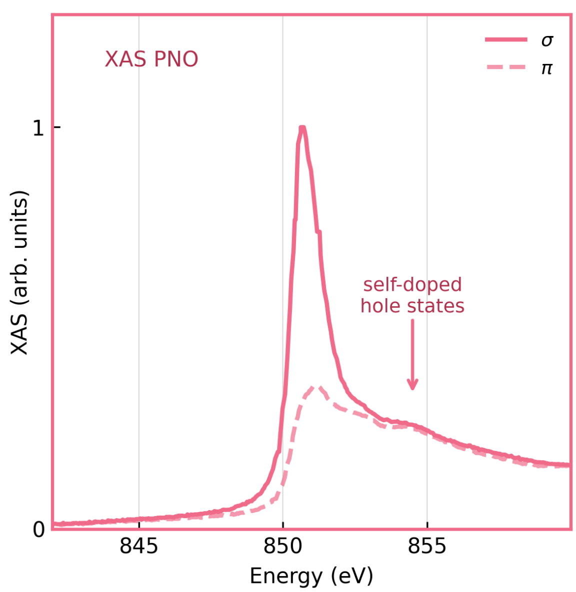

Supplementary Fig. 1. Ni L-edge X-ray absorption spectroscopy (XAS) for $PrNiO_2$. Measurements were performed at 16 K with a grazing-in angle ($\theta = 10°$). Linear vertical (σ) and horizontal (π) incident light are indicated by solid and dashed lines.

II. FITTING OF RIXS SPECTRA

In Supplementary Fig. 2(a) we plot the RIXS spectrum of the amorphous carbon tape. The experimental energy resolution is determined to be 39 meV (full-width-at-half-maximum, FWHM) by fitting this data using a single Gaussian profile. In Supplementary Fig. 2(b), we overlay the same Gaussian profile on a representative RIXS spectrum of $PrNiO_2$. This Gaussian resolution function cannot fully capture the signal profile around $0 \sim 50\,\mathrm{meV}$, which implies the necessity to include a phonon mode at approximately 35 meV. Another phonon mode is identified at around 70 meV. The two phonon modes have been previously observed in high-resolution RIXS measurements of cuprates [3, 4] and have been attributed respectively to the bond-buckling (lower energy) and bond-stretching (higher energy) phonons, given their significant coupling to electrons.

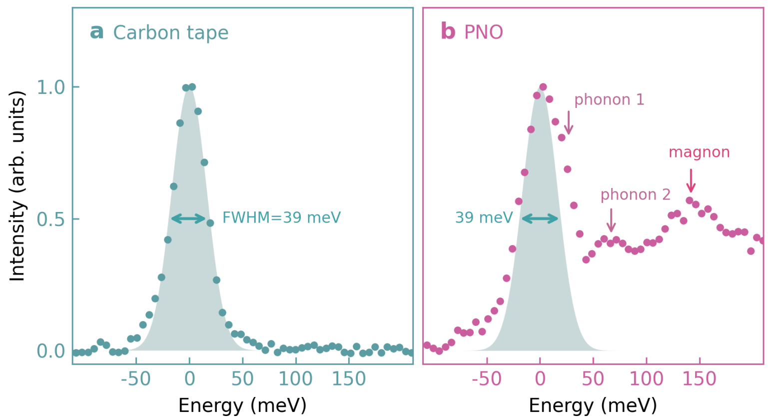

Supplementary Fig. 2. (a) RIXS spectrum on carbon tape. The shaded area denotes the best-fit Gaussian profile. (b) RIXS spectrum on $PrNiO_2$, The shaded area denotes a Gaussian function with FWHM determined in (a). Both spectra are normalized to the maximum intensity.

Therefore the low-energy part (-100 to 450 meV) of RIXS spectra of $PrNiO_2$ are fitted using a five-component model:

$$F(x) = G_1(x) + G_2(x) + G_3(x) + D(x) + \mathrm{Bg}(x), \tag{1}$$

where $G_i(x)$ is a Gaussian profile:

$$G_i(x) = I_i \exp\left\{-\frac{(x-x_i)^2}{2\sigma^2}\right\}, \tag{2}$$

with I_i and x_i being free parameters, and the standard deviation $\sigma = 16.6\,\mathrm{meV}$ fixed by instrumental resolution ($\mathrm{FWHM} = 39\,\mathrm{meV}$). They are used to model the elastic signal and two phonon modes. $D(x)$ is a damped harmonic oscillator function modified by the Bose factor and convolved with the energy resolution:

$$D(x) = (f * G)(x), \quad f(x) = \underbrace{\frac{A}{(x^2-\omega_0^2)^2 + (\gamma x)^2}}_{\text{damped harmonic oscillator}} \times \left(\underbrace{\frac{1}{\exp\left(\frac{x}{k_\mathrm{B}T}\right) - 1}}_{\text{Bose factor}} + 1 \right), \tag{3}$$

where the operator $*$ stands for convolution, $G(x)$ is the resolution function, A, ω_0, and γ are free parameters, and T is the temperature. In the main text, the parameter $\omega_1 = \sqrt{\omega_0^2 - \gamma^2/4}$ is termed the damped energy. This function $D(x)$ models the magnon excitations. The residual background is captured by a quadratic function denoted by $\mathrm{Bg}(x)$.

Two exemplary RIXS spectra and the fits are shown in Supplementary Fig. 3. It is worth mentioning that the sharp feature at $Q = (0.1, 0)$ (as shown in Supplementary Fig. 3(a)) at $\sim$80 meV can be attributed to the optical phonon mode, labeled as phonon 2 in the figure. This can be seen by further looking at a higher $Q = (0.25, 0)$ (Supplementary Fig. 3(b)) where the magnon signal moves to a higher energy, while the peak-like signal, though weaker, still remains at a similar energy $\sim$80 meV.

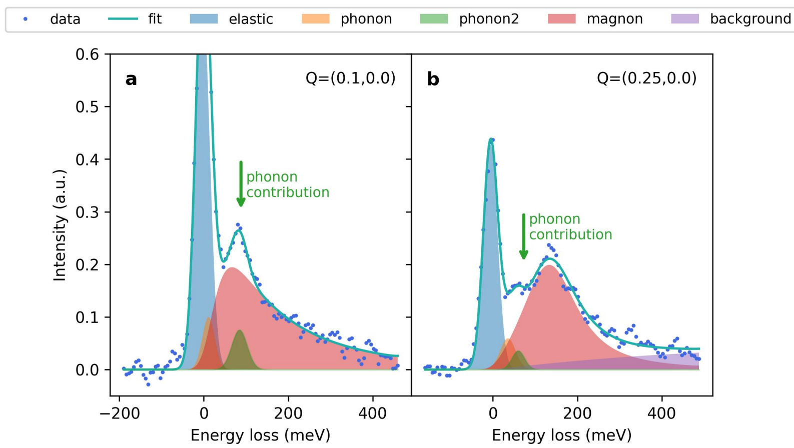

Supplementary Fig. 3. RIXS spectra recorded with π polarization on PrNiO2 at indicated Q points. The fitting components are also plotted on top of the data points. The green arrow indicates the optical phonon's contribution to the peak-like feature at $\sim$80 meV.

Supplementary References

[1] M. Rossi, H. Lu, A. Nag, D. Li, M. Osada, K. Lee, B. Y. Wang, S. Agrestini, M. Garcia-Fernandez, J. J. Kas, Y.-D. Chuang, Z. X. Shen, H. Y. Hwang, B. Moritz, K.-J. Zhou, T. P. Devereaux, and W. S. Lee, Phys. Rev. B **104**, L220505 (2021).

[2] Q. Gao, S. Fan, Q. Wang, J. Li, X. Ren, I. Biało, A. Drewanowski, P. Rothenbühler, J. Choi, R. Sutarto, Y. Wang, T. Xiang, J. Hu, K.-J. Zhou, V. Bisogni, R. Comin, J. Chang, J. Pelliciari, X. J. Zhou, and Z. Zhu, Nat. Commun. **15**, 5576 (2024).

[3] X. Hong, Y. Yan, L. Martinelli, I. Biało, K. v. Arx, J. Choi, Y. Sassa, S. Pyon, T. Takayama, H. Takagi, Z. Li, M. Garcia-Fernandez, K.-J. Zhou, J. Chang, and Q. Wang, arXiv:2503.04334 (2025).

[4] L. Martinelli, I. Biało, X. Hong, J. Oppliger, C. Lin, T. Schaller, J. Küspert, M. H. Fischer, T. Kurosawa, N. Momono, M. Oda, D. V. Novikov, A. Khadiev, E. Weschke, J. Choi, S. Agrestini, M. Garcia-Fernandez, K.-J. Zhou, Q. Wang, and J. Chang, Phys. Rev. B **112**, L041124 (2025).